Mechanical, Corrosion, and Wear Properties of TiZrTaNbSn Biomedical High-Entropy Alloys

Xiaohong Wang [1], Tingjun Hu [1], Tengfei Ma [1], Xing Yang [1], Dongdong Zhu [1], Duo Dong [1], Junjian Xiao [1,*] and Xiaohong Yang [2,3,*]

1   Key Laboratory of Air-Driven Equipment Technology of Zhejiang Province, Quzhou University, Quzhou 324000, China
2   Academician Expert Workstation, Jinhua Polytechnic, Jinhua 321017, China
3   Key Laboratory of Crop Harvesting Equipment Technology of Zhejiang Province, Jinhua 321017, China
*   Correspondence: xjj919@sohu.com (J.X.); jhyxh656593@163.com (X.Y.); Tel.: +86-139-6703-9758 (J.X.); +86-180-9126-9296 (X.Y.)

Abstract: The phase composition, microstructure, mechanical, corrosion, and wear behaviors of the Ti15Zr35Ta10Nb10Sn30 (Sn30) and Ti15Zr30Ta10Nb10Sn35 (Sn35) biomedical high-entropy alloys (BHEAs) were studied. We found that the Ti–Zr–Ta–Nb–Sn BHEAs showed hyper-eutectic and eutectic structures with body-centered cubic (BCC) and face-centered cubic (FCC) solid-solution phases. The Sn30 BHEA exhibited a high Vickers hardness of approximately 501.2 HV, a compressive strength approaching 684.5 MPa, and plastic strain of over 46.6%. Furthermore, the Vickers hardness and compressive strength of Sn35 BHEA are 488.7 HV and 999.2 MPa, respectively, with a large plastic strain of over 49.9%. Moreover, the Sn30 and Sn 35 BHEA friction coefficients are 0.152 and 0.264, respectively. Sn30 BHEA has the smallest and shallowest furrow-groove width, and its wear rate is 0.86 (km/mm^3); at the same time, we observed the delamination phenomenon. Sn35 BHEA has a wear rate value of 0.78 (km/mm^3), and it displays wear debris and the largest–deepest furrow groove. Sn30 BHEA has the highest impedance value, and its corrosion current density I_{corr} is 1.261×10^{-7} (A/cm^2), which is lower than that of Sn35 BHEA (1.265×10^{-6} (A/cm^2)) by 88%, and the passivation current density I_{pass} of Sn30 BHEA and Sn35 BHEA is 4.44×10^{-4} (A/cm^2) and 3.71×10^{-3} (A/cm^2), respectively. Therefore, Sn30 BHEA preferentially produces passive film and has a small corrosion tendency, and its corrosion resistance is considerably better than that of the Sn35 BHEA alloy.

Keywords: biomedical high entropy alloy; TiZrTaNbSn; corrosion resistance; mechanical properties; friction and wear

1. Introduction

Pure Ti has the advantages of non-toxicity, light weight, high strength, good biocompatibility, etc. Therefore, in the 1950s, the United States and the United Kingdom started to apply it for use with living organisms [1]. In the 1960s, Ti alloys (first Ti-6A1-4V [2,3] and later Ti-5Al-2.5Fe and Ti-6A1-7Nb) began to be widely used in clinical practice as a human implant material [4–7]. In the 1970s and 1980s, researchers began to prepare Ti alloys with V-free implants because of its toxic and potentially harmful effects on the human body; furthermore, in the mid-1980s, new types of α+β Ti alloys, namely Ti-5Al-2.5Fe and Ti-6Al-7Nb, were developed in Europe [3]. The mechanical properties of these alloys are similar to Ti-6Al-4V [7], albeit with higher biocompatibility and corrosion resistance properties. However, these alloys still contain Al, which can cause organ damage and harmful symptoms, such as osteomalacia, anemia, and neurotin disorder [4,5]. Based on the above reasons, new types of alloys, which are free of both V and Al but with the addition of Nb, Zr, Ta, and Sn (Ti-13Nb-13Zr, Ti-35Nb-5Ta7Zr, Ti-24Nb-4Zr-7.9Sn), have been developed in recent years [4–6], and their elastic moduli are closer to that of natural

human bone, and their strength is also higher than that of pure Ti. Consequently, Ti alloys are being rapidly developed for human implant materials; however, their strength, friction and wear, and corrosion resistance need to be studied further.

Traditional alloy systems usually consist of one or two main elements, and the content of the other elements is much lower. In 2004, Yeh et al. [8–10] first proposed high-entropy alloy, a class of materials containing five or more elements in relatively high concentrations (5–35 at.%) [11,12]. Due to their unique high-entropy, sluggish diffusion, lattice distortion, and cocktail effects [13–15], HEAs show excellent comprehensive properties compared with traditional alloys, such as high hardness [16], high strength [17], corrosion resistance, wear resistance [18,19], etc. At the same time, high-entropy alloys break the traditional alloy design concept of using only one principal element. Despite this, researchers are actively exploring the possibility of applying high-entropy alloys in new products [20], such as biomedical, magnetic, hydrogen storage materials, etc. [21–25]. At present, the comprehensive mechanical properties of medical alloys are still to be improved in clinical practice. Therefore, the design concept of high-entropy alloy can be used to prepare biomedical high-entropy alloy materials with low modulus, high strength, corrosion resistance, and other excellent comprehensive properties to meet demand.

In the past decade, a series of Ti-Zr-Hf-Nb-Ta [21–25], Ti-Mo-Ta-Nb-Zr [26–29], and Ti-Nb-Hf-Ta-Zr-Mo [30,31] HEAs with considerable mechanical and chemical properties suitable for biomedical applications have been designed. Researchers are also improving the performance of HEAs by alloying with O, Si, Al, and Cr [32–35]. However, we noticed that adding Sn to Fe-Co-Cu-Ni(-Mn) HEAs can improve elongation strain and tensile strength by 16.9% and 476.9MPa, respectively [36,37]. In addition, Sn is non-cytotoxic and widely present in β-Ti alloys [38–41]. Previously, we studied the effects of atomic ratios on as-cast microstructural evolution, and the mechanical and electrochemical properties of Ti30Zr20Ta20Nb20Sn10 high-entropy alloy [42]. While its elastic modulus is relatively high, with a value of 110GPa, it does not match the elastic modulus of human bones (30–50 GPa). Moreover, Zr-based $Ti_{0.5}Zr_{1.5}Ta_{0.5}NbSn_{0.2}$ (Ti13.5Zr40.5Ta13.5Nb27Sn5.5) high-entropy alloys display an elastic modulus value of about 40 GPa [43]. Therefore, in our study, we designed a new Zr-based high-entropy Ti-Zr-Ta-Nb-Sn alloy based on metastable β-titanium alloy, which is based on the four elements of Ti-Zr-Ta-Nb. We prepared two kinds of biomedical-grade high-entropy alloys, namely Sn30 BHEA and Sn35 BHEA, by vacuum arc melting, and we systematically studied the feasibility of preparing biomedical-grade high-entropy alloy with five elements (Ti, Zr, Ta, Nb, and Sn), paying specific attention to morphology, compressive strength, electrochemical corrosion, and friction and wear properties. Our work will provide data for the future development of biomedical-grade high-entropy alloy, in addition to guidance for further scientific research on Ti alloys.

2. Experimental

The Ti, Zr, Ta, Nb, and Sn raw materials with a purity of more than 99.9 wt.% were used to prepare BHEAs with the atom ratio of Sn30 BHEA and Sn35 BHEA. The master alloy ingot was arc melted and cooled on a water-cooled copper crucible in a high-purity argon protective atmosphere at least 5 times to ensure the chemical homogeneity. Wire cut electrical discharge machining (WEDM, DHL-500) was used to cut samples from the core region of the master alloy ingot (Buttonhole, maximum diameter Φ32mm, maximum height 16 mm). The surface of the alloy sample was ground with silicon carbide sandpaper up to 2000 grit. The phase composition and microstructure of the alloy sample were characterized via an X-ray diffractometer (XRD, Rigaku D/max-RB) and a Hitachi S-4300 scanning electron microscope and HITACHI SU8010 scanning electron microscope (SEM), and energy dispersive X-ray spectroscopy (EDS) was used to analyze the chemical composition of the HEAs.

Cylinder-shaped (Φ4 mm × 6 mm) samples were cut via WEDM, and used for Vickers hardness and room-temperature compression stress and strain test. The microhardness test was carried out on an HYHVS-1000T Vickers hardness tester using an applied load of

1000 g force (gf) and a dwell time of 15 s. A 370.1 type mechanical testing system (MTS) was employed to record the room-temperature compression stress and strain curves of HEA samples. The compressive strain rate was set as 0.5 mm/min. After the compression test, the lateral surface morphologies of the compressed specimens were examined by SEM.

Corrosion behavior was obtained through the electrochemical workstation (CHI660E) using a three-electrode-cell system. Saturated mercuric chloride was used as reference electrode, platinum electrode as counter electrode, a 1 mm thick sample was embedded in copper wire as working electrode, test temperature was 26 °C, scanning speed was 1 mV/s, and scanning voltage range was from −1.5 to +1.5 V. Before corrosion experiments, the surface of the sample was polished with 2000 grit silicon carbide sandpapers. Then, as-polished specimens were ultrasonically cleaned in deionized water, acetone, and ethanol. Before the potentiodynamic polarization test, the alloy sample was immersed in 3.5% NaCl solution until the open circuit potential (OCP) reached a stable state. After the polarization experiment, TAFEL and IMP were used to measure the polarization curve and AC impedance of Sn30 and Sn35 BHEAs, respectively. Then, Corrview software was used to analyze the Tafel curve and Zview software to analyze the impedance spectrum. The corroded morphologies on the sample surface were examined by SEM, and the composition of the corroded surface was determined by EDS.

When performing the friction and wear test, we ensured each specimen of the two materials was wet-ground and polished using a polishing machine (UNIPOL-1502, Shenyang Kejing Auto-Instrument Co., Ltd., Shenyang, China) with a series of silicon carbide papers of P320, P400, P800, P1200, P1500, P2000, and P3000 grits (Matador Starcke, Germany) under water cooling. Finally, after ultrasonically cleaning for 10 min in deionized water, we fine-polished all specimens with a diamond velour polishing pad under a flowing cerium oxide solution (particle size: 1.5 μm) (Shenyang Kejing Auto-Instrument Co., Ltd., China) before finishing with a mirror-like surface. Then, we tested the wear behaviors of the HEAs by a VHX-2000 tribology tester using a Si_3N_4 ball (4 mm in diameter) as the couple-pair. In our study, the test parameters were as follows: load 10 N, time of 30 min, sliding velocity 600 r/min, and friction reciprocating motion amplitude 2 mm. We recorded the friction coefficient during the sliding process. After the wear test, we determined the wear volume (W_V) of the alloy samples by an MT-500 Probe-type material surface profile measuring instrument. We examined the morphologies and compositions of the HEAs' wear scars by SEM and EDS, respectively.

3. Results

3.1. Phase Composition and Microstructure of Sn30 BHEA and Sn35 BHEA

Figure 1 shows the XRD diffraction patterns of Sn30 BHEA and Sn35 BHEA. We found that there is an obvious peak correspondence relationship by comparing with the standard PDF database. The diffraction peaks of 36.8° and 38.4° correspond to BCC Zr, FCC Nb, and BCC Ti solid solutions, respectively. At the same time, 64.8° corresponds to the FCC Ti solid solution, while 75.9° and 80.2° correspond to the diffraction peaks of the BCC Zr and BCC Ti solid solutions, respectively. We also observed that 41.8° corresponds to the diffraction peak of the BCC Ti solid solution in Sn30 BHEA. Furthermore, the 37.6° (Sn35 BHEA) and 35.9° (Sn30 BHEA) diffraction peaks correspond to the HCP Zr_5Sn_3 phase. Our results show that both alloys contain BCC and FCC phases. Table 1 shows the corresponding thermodynamic parameters. The values of ΔH, ΔS, and δ are in the range where the solid-solution phase is likely to occur. Table 1 shows the calculated values of the entropy–enthalpy quotient parameter (Ω), the valence electron concentration (VEC) criterion, and the mean square deviation of the atomic radius of elements (δ) of these two high-entropy alloys. The thermodynamic parameter VEC further proves that FCC and BCC phases co-exist in the alloy.
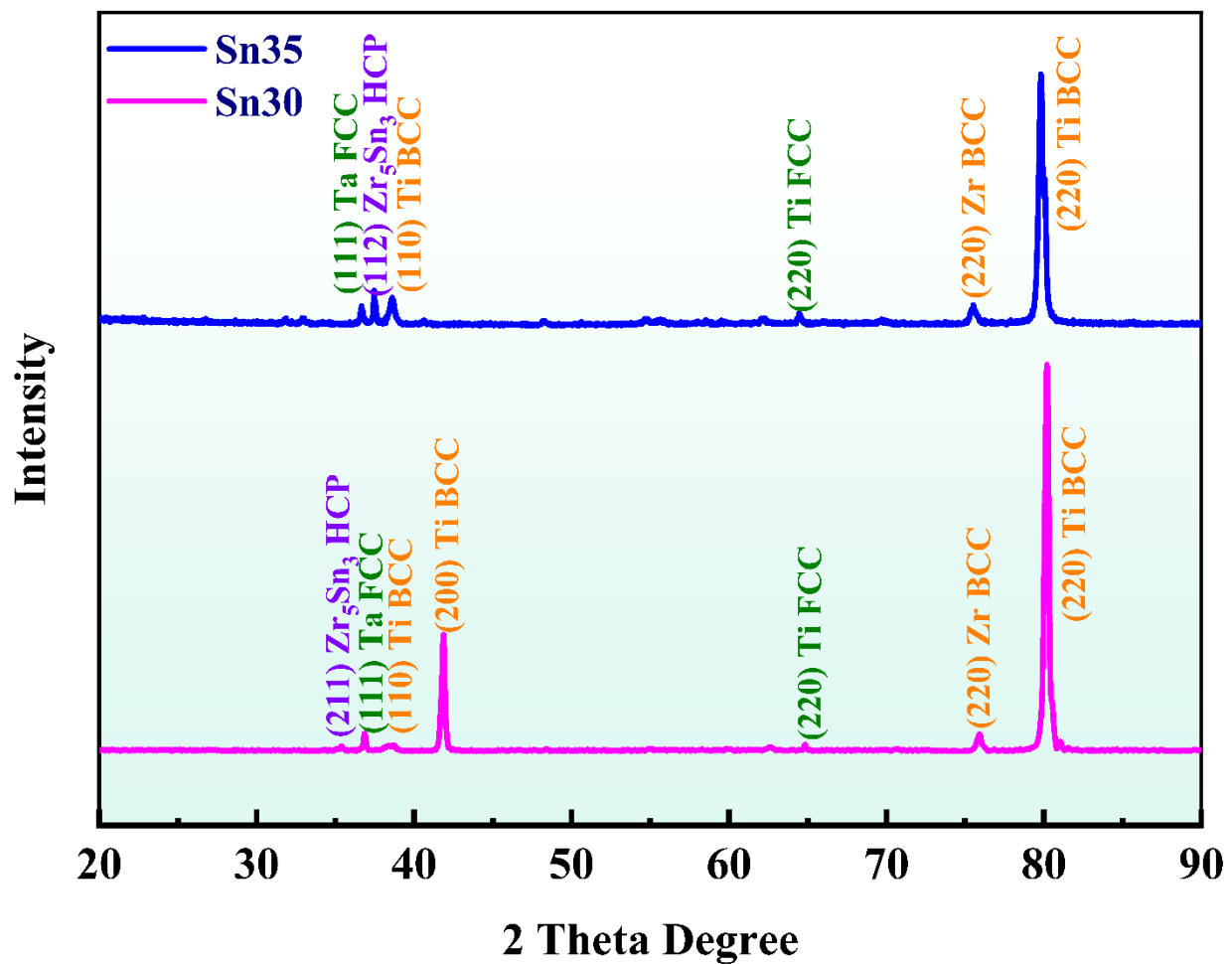
Figure 1. XRD patterns of Sn30 BHEA and Sn35 BHEA.

Table 1. Thermodynamic parameters of Sn30 BHEA and Sn35 BHEA.

Alloy	Ω	δ	ΔH/(KJ/mol)	ΔS/J (K/mol)	VEC
Sn30 BHEA	1.04	3.78	−21.2	12.25	7.2
Sn35 BHEA	0.95	3.64	−22	12.3	7.7

We used SEM and EDS to analyze the chemical compositions and microstructures of HEAs. Figure 2 shows the microstructures of Sn30 BHEA and Sn35 BHEA. Sn30 BHEA is a typical hypoeutectic structure composed of long-strip gray phases, a bright white small-block phase, and an interphase rod eutectic microstructure (Figure 2a,b). Moreover, the eutectic microstructure's volume fraction is 33.8%. Sn35 BHEA is a typical eutectic microstructure with lamellar distribution; however, there are some bright white blocky phases distributed on the dark gray phase. Additionally, the solidification mode looks more equiaxed for Sn35 BHEAs, while it seems more columnar dendritic for Sn30 BHEAs. With changes in atomic ratio, the eutectic structure's content and morphology also considerably changed. In order to analyze the element content of each phase in Figure 2, EDS analysis was carried out on eutectic microstructure (area 1), gray phases (area 2), and bright white blocky phases (area 3). The results are shown in Table 2. We discovered a high content of Zr and Sn in the dark gray phase of both high-entropy alloys. Combined with our XRD analysis results, we deduced that this phase is a Zr solid solution with a BCC crystal structure. The bright-colored small-block area contains a large amount of Ti and Ta, which exceeds the initial composition of the alloy; therefore, it is rich in Ta and Ti FCC phase.

Based on our above analysis, we determined that the bright-colored phase in the remaining eutectic structure is a Ti solid-solution phase with a BCC crystal structure.
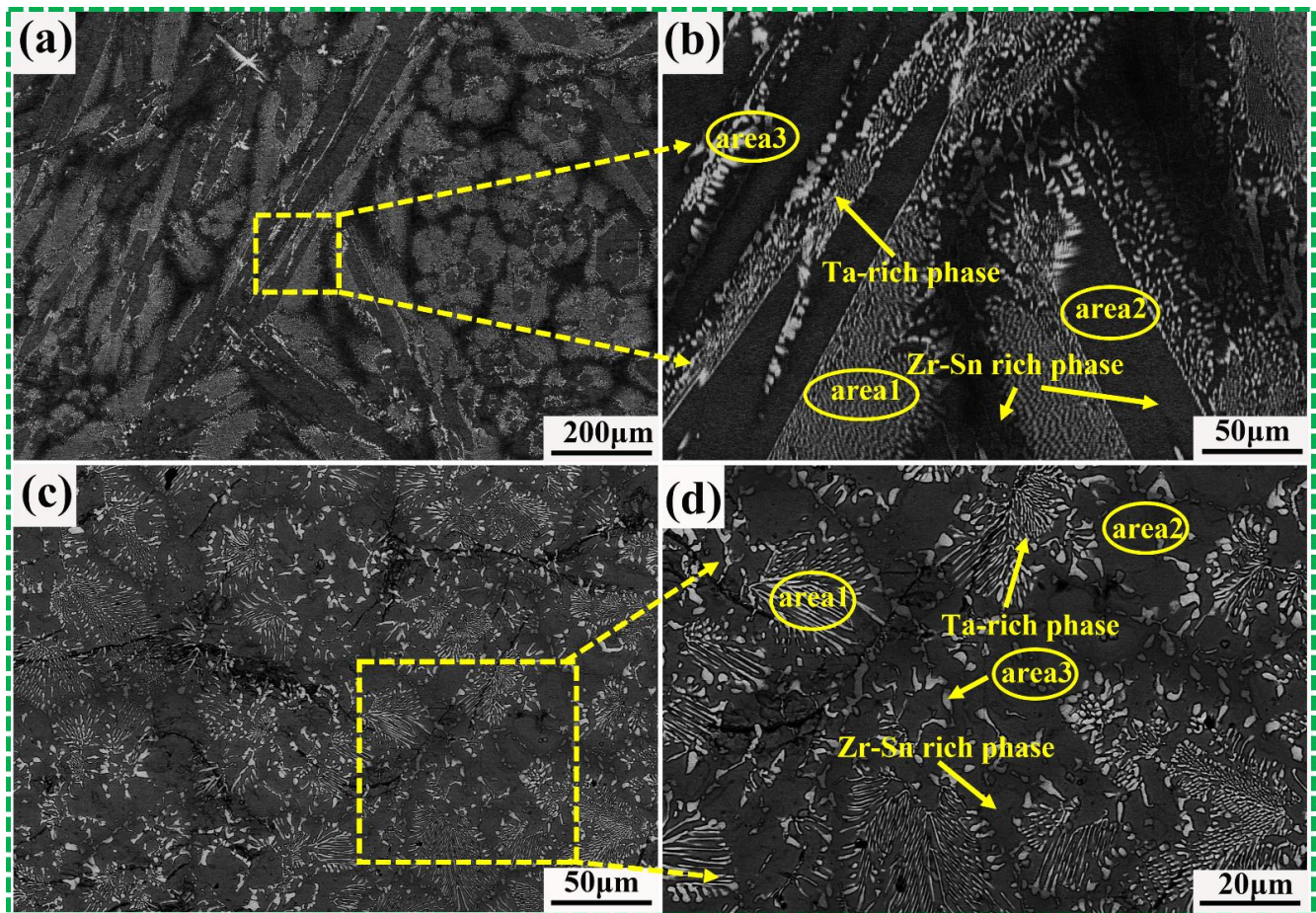

Figure 2. The microstructure of Sn30 BHEA and Sn35 BHEA. (**a**,**b**) Sn30 BHEA, (**c**,**d**) Sn35BHEA.

Table 2. EDS analysis of the phase in Figure 2.

Composition	Place	Color	Ti/at%	Zr/at%	Ta/at%	Nb/at	Sn/at%
	area 1	-	19.51	26.56	8.21	16.80	28.93
Sn30 BHEA	area 2	Gray	15.96	39.71	3.75	8.52	32.06
	area 3	Bright white	28.69	19.14	12.07	15.38	24.72
	area 1	-	19.58	27.83	7.82	20.02	24.73
Sn35 BHEA	area 2	Gray	15.69	34.01	0.98	8.83	40.50
	area 3	Bright white	24.55	18.39	14.65	14.55	27.86

To further analyze the element distribution, the map scanning results of its element distribution are shown in Figure 3. Figure 3 shows the map scanning results of the element distribution. The Zr, Nb, and Sn elements are mainly distributed in the dark gray phase, while Ti tends to be uniformly distributed in the dark gray phase, and is eutectic in structure; however, Ti is segregated in the bulk phase close to the eutectic microstructure (Figure 3(a1–a5)). For Sn35 BHEA, the distribution of elements tends to be consistent with that of Sn30 BHEA.
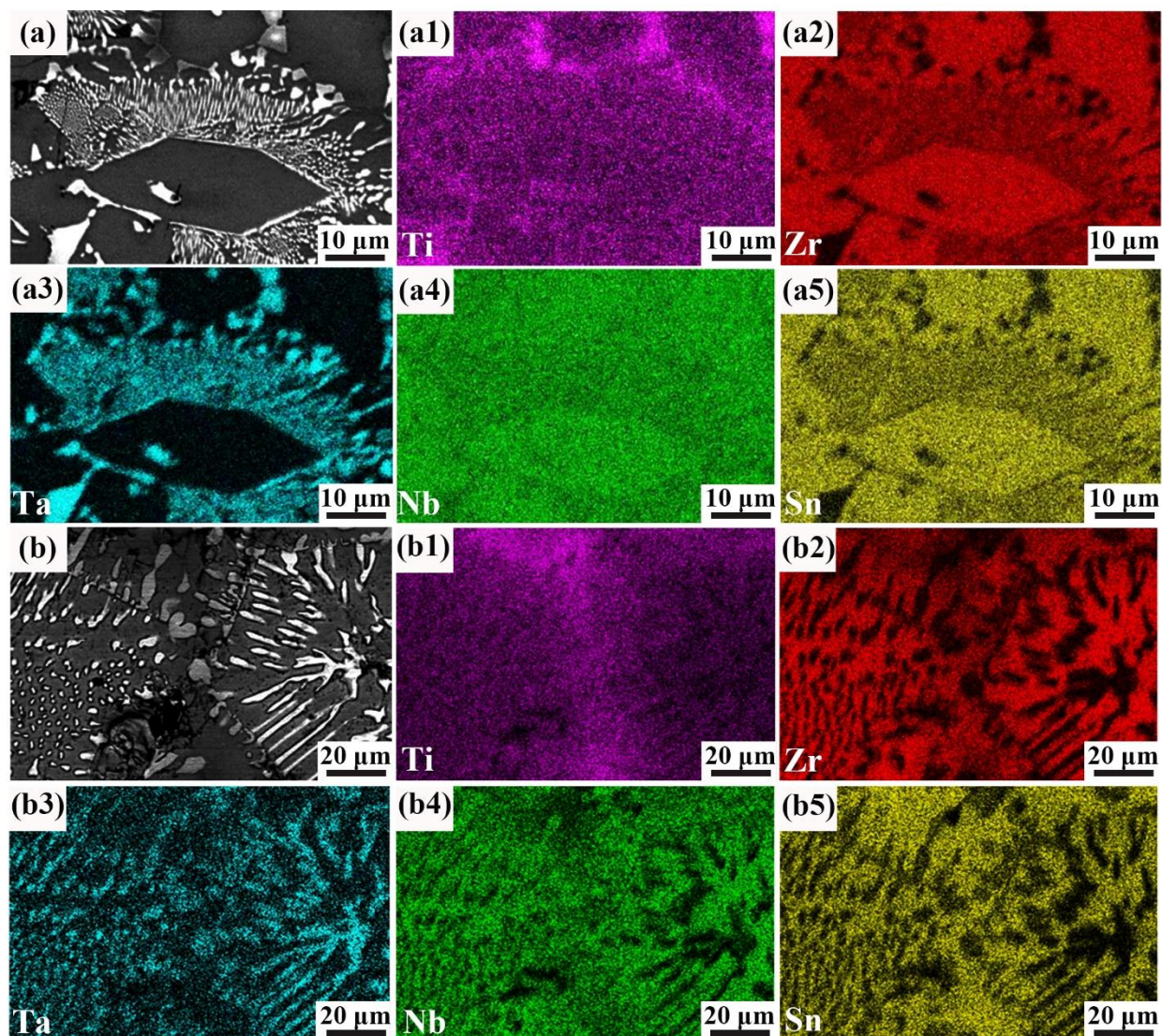
Figure 3. The map scanning of Sn30 BHEA and Sn35 BHEA: (**a**)–(**a5**) Sn30 BHEA, (**b**)–(**b5**) Sn35 BHEA.

3.2. Mechanical Properties of Sn30 BHEA and Sn35 BHEA

The mechanical properties of Sn30 BHEA and Sn35 BHEA are shown in Figures 4 and 5. Figure 4a shows the compression stress–strain curves of Sn30 BHEA and Sn35 BHEA at room temperature. Compared with Sn35 HEAs, the Sn30 HEAs exhibit double-yielding behavior, which is often observed in shape memory alloys as a stress-induced phase transformation and has relatively lower plasticity [44]. Figure 4b displays the Vickers hardness results for both alloys. Hardness is one of their mechanical properties, and it has a considerable impact on the application of alloys. At the same time, it is also one of the factors that affect alloys' friction and wear properties. Sn30 HEA has the highest hardness level, and the average value of 5 measurements is 501.2HV, while the hardness of alloy Sn35 HEAs is 488.72HV, which is slightly lower. Figure 4c–f show the fracture morphologies of these two high-entropy alloys after compression testing. Figure 4c,d show that Sn30 BHEA's macrofracture morphology is relatively flat, while its micromorphology has river patterns, showing obvious shear failure characteristics. On the gray strip, it also shows typical brittle fracture characteristics. Furthermore, after increasing the magnification, we observed tear edges and dimples on the eutectic structure, showing the mixed characteristics of quasi-cleavage and ductile fractures. Generally, the samples show brittle quasi-cleavage fractures [45]. Figure 4e,f show that the compression fracture surfaces of Sn35 HEAs are uneven and considerably fluctuate, and there are obvious signs

of shear tear on the fractures. After increasing the magnification, we observed shallow and slender dimples on the relatively flat shear plane, and we determined that the compression fracture is generally a brittle cleavage fracture. Figure 5 shows the maximum strain and compressive strength values corresponding to the two alloys. The maximum strain value and compressive strength of Sn30 HEAs are 46.6% and 684.5 MPa, respectively, and the maximum strain value and compressive strength of Sn35 HEAs are 49.9% and 999.2 MPa, respectively. Therefore, Sn35 HEAs exhibit better mechanical properties.
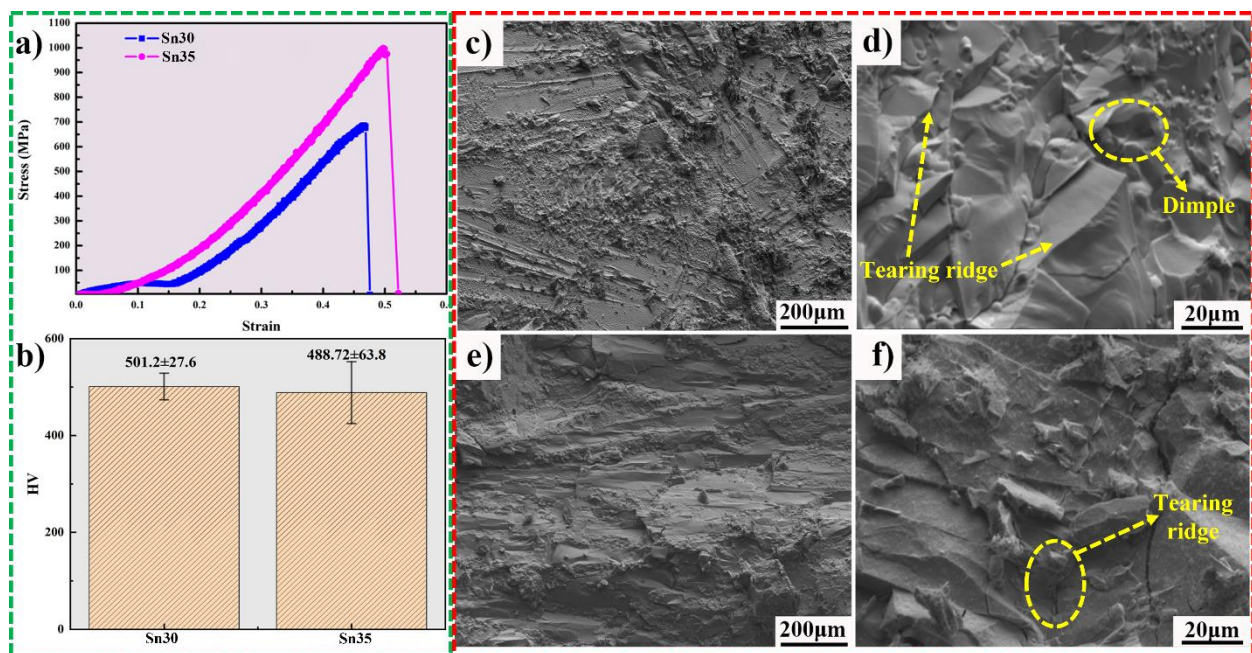

Figure 4. Compressive stress–strain curves and corresponding fracture morphologies of Sn30 BHEA and Sn35 BHEA: (**a**) stress–strain curves, (**b**) HV of Sn30 BHEA and Sn35 BHEA, (**c**,**d**) fracture morphology of Sn30 BHEA, (**e**,**f**) fracture morphology of Sn35 BHEA.
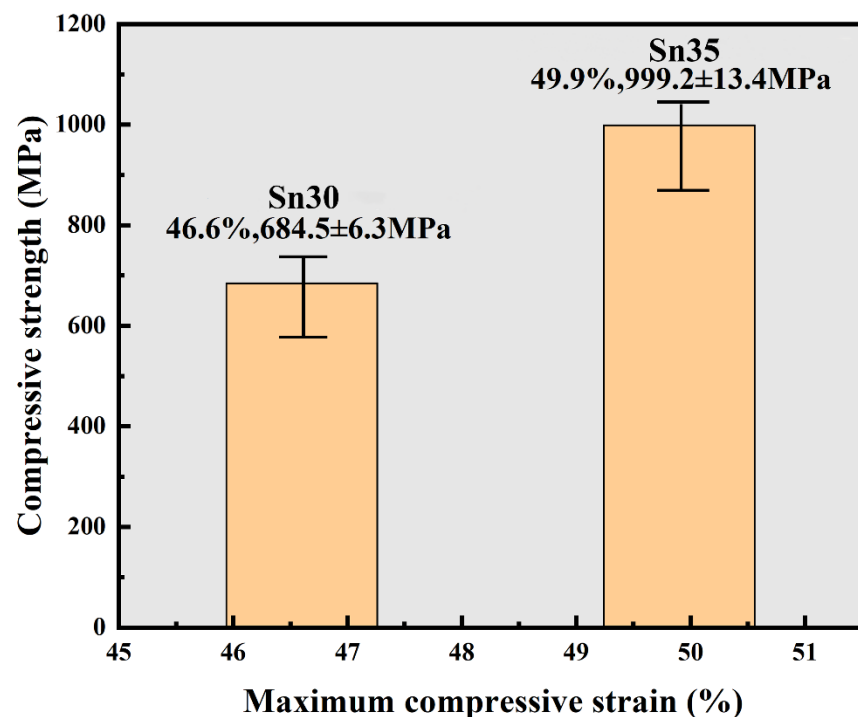

Figure 5. Compression properties of Sn30 BHEA and Sn35 BHEA.

3.3. Friction and Wear Properties of Sn30 BHEA and Sn35 BHEA

As hardness is one of the primary factors that affect the friction and wear properties of the alloys, there are certain requirements regarding the friction and wear properties of materials implanted into the human body. The friction and wear mechanical properties tests of Sn30 BHEA and Sn35 BHEA are shown in Figure 6. Wear marks can be clearly seen in Figure 6a, which shows the sample used in the friction and wear test, including its wear marks and approximate dimensions. Figure 6b displays the friction coefficient curves (COFs). The COFs of Sn30 and Sn35 are 0.152 and 0.264, respectively. Moreover, the friction coefficients first display a sharp increase and then decrease before becoming flat. The main reason is that at the initial stage, the sample and the Si_3N_4 sphere will undergo a point-to-surface contact process. First, the friction coefficient is sensitive to the roughness of the sample surface, causing the friction coefficient to rapidly increase. When the ball makes complete contact with the sample and the contact condition is stable, the friction coefficient tends to be flat. The Sn30 BHEA presented the minimum average COFs. The mechanical properties (hardness, strength, and plasticity) have a considerable effect on tribological properties [46–48]. Normally, the relationship between tribological and mechanical properties can be described as $W = k(P/H)$ (W is wear rate, P is applied load, k is relative to plasticity, and H is hardness) [46]. Figure 4 shows there are no considerable differences in plasticity; however, Sn30 BHEA's hardness is much higher. Hence, the tribological properties of Sn30 BHEA are superior to Sn35 BHEA.
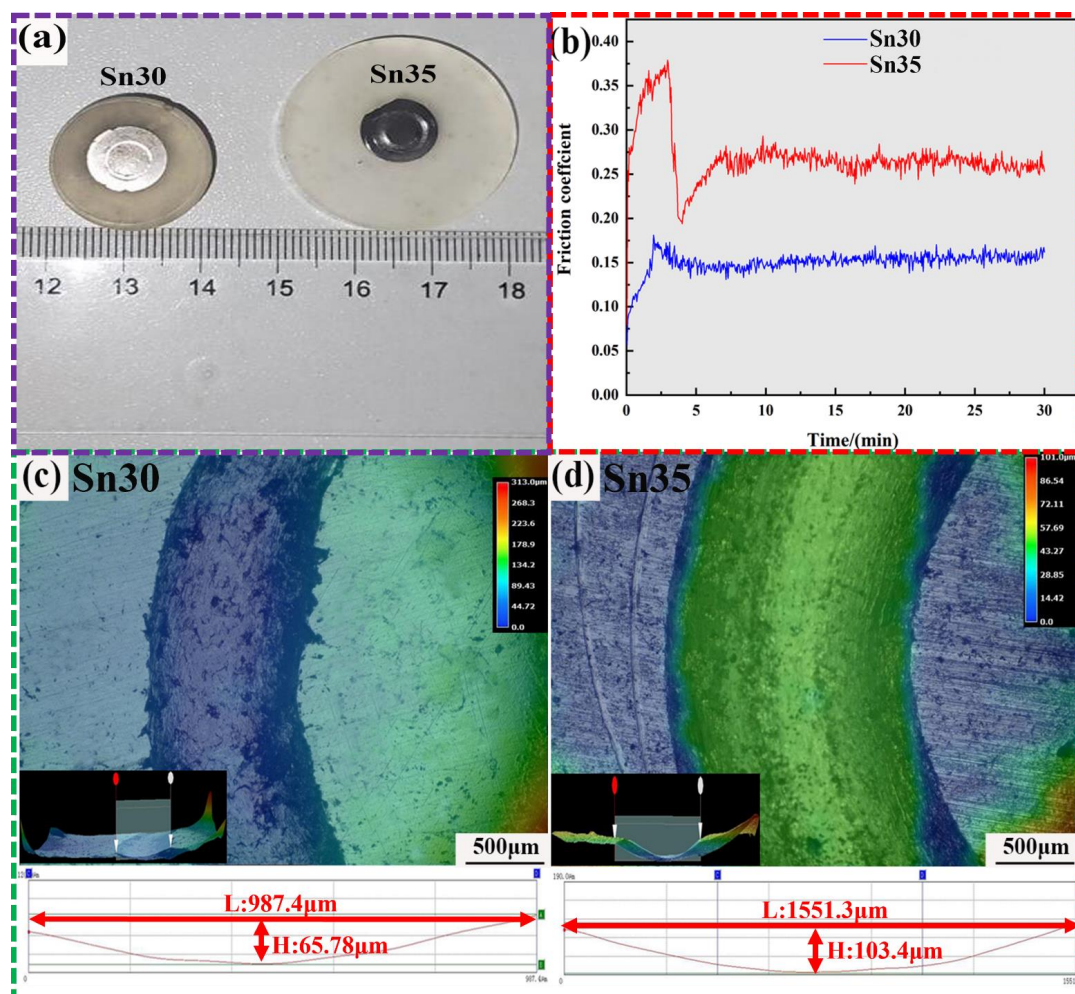

Figure 6. Friction and wear test results of Sn30 BHEA and Sn35 BHEA (**a**) samples, (**b**) friction coefficient curves, and profiles of the worn surfaces for sintered composites and corresponding 2D cross-section profiles of wear tracks: (**c**) Sn30 BHEA, (**d**) Sn35 BHEA.

To further obtain the wear volume (W_v) of the Sn30 BHEA and Sn35 BHEA after the wear test, the section profile morphologies of the worn surfaces were characterized by a Keyence surface profilometer (VHX-2000), and the results are illustrated in Figure 6c,d. Sn30 BHEA showed finer grooves owing to its higher hardness; therefore, it resists abrasive wear (Figure 6c). Abrasive wear was aggravated in Sn35 BHEA, which was confirmed by its widened grooves (Figure 6d). The corresponding wear width and depth in Figure 6a can be obtained directly from the images. Table 3 displays the calculated wear properties, where E is wear resistance, K_v is specific wear rate, and K_2 is linear wear rate. The Kv of Sn30 BHEA is 2.27×10^{-4} (mm^3/nm), the K_2 is 1.163 (mm^3/km), E is 0.86 (km/mm^3), and the W_v is 0.51 mm^3. Furthermore, the Kv of Sn35 BHEA is 2.49×10^{-4} (mm^3/nm), and the values of K_2, E, and W_v are 1.277 (mm^3/km), 0.78 (km/mm^3), and 0.56 mm^3, respectively. A higher material loss rate will also lead to slight work hardening (Figure 7). Therefore, our comprehensive analysis shows that Sn30 BHEA has better friction and wear morphologies.

Table 3. Wear properties of Sn30 BHEA and Sn35 BHEA at room temperature.

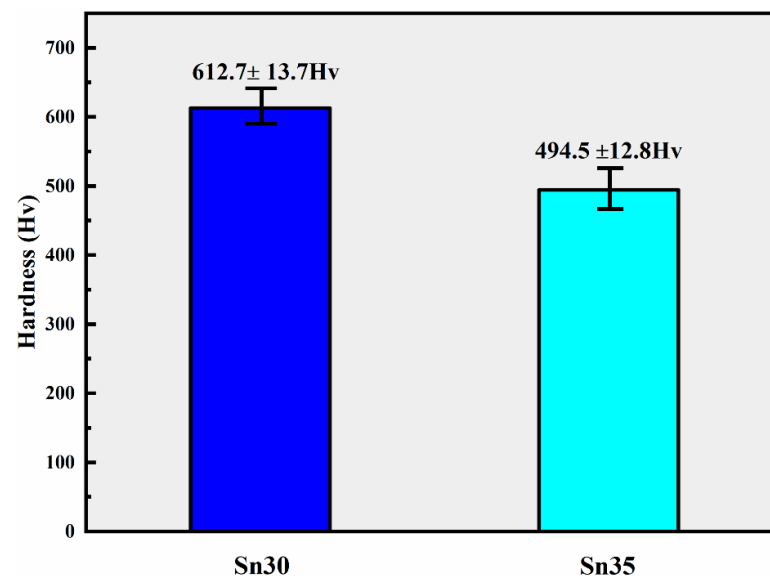| Sample	L/m	W_v/(mm^3)	K_v/(mm^3/nm)	K_2/(mm^3/km)	E/(km/mm^3)
Sn30 BHEA	226.2	0.51	2.27×10^{-4}	1.163	0.86
Sn35 BHEA	226.2	0.56	2.49×10^{-4}	1.277	0.78

Figure 7. Hardness of the worn surface for the Sn30 BHEA and Sn35 BHEA.

We carried out our SEM characterizations of the worn surfaces to explore the wear mechanisms of Sn30 BHEA and Sn35 BHEA, the results are displayed in Figure 8, and the plastic deformation and delamination traces showed severe wear for both alloys. Furthermore, the wear surfaces of all Sn30 BHEAs and Sn35 BHEAs showed typical furrow characteristics, and there are grooves and wear debris along the sliding direction due to the micro cutting and furrow effects of the Si_3N_4 ball, which indicates that furrow wear is the main wear mechanism [47,49].
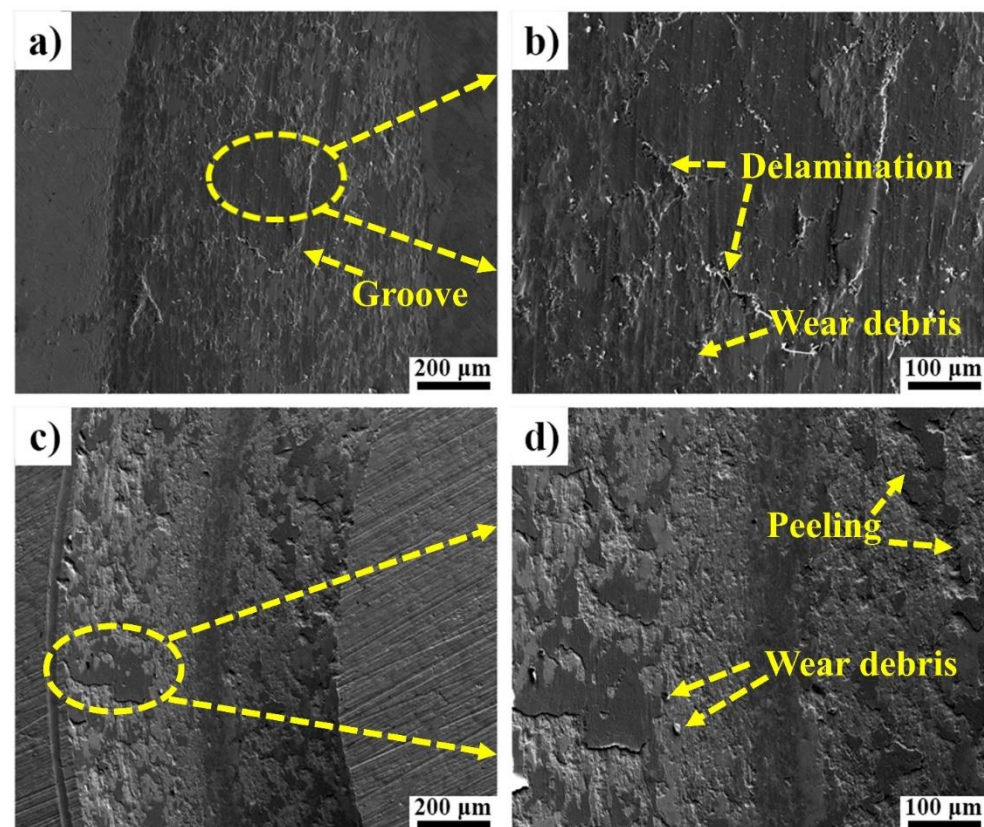
Figure 8. SEM images of Sn30 BHEA and Sn35 BHEA: (**a,b**) Sn30 BHEA, (**c,d**) Sn35 BHEA.

Sn30 BHEA's worn surfaces were smoother with less debris and smaller grooves compared with Sn30 BHEA, as shown in Figure 8a–d. Moreover, Figure 8a shows that the surface morphology of the Sn30 BHEA alloy's friction structure tends to form a regular pit structure, and the wear surface is almost free of wear debris. Figure 8c,d show that there are wear debris generated on Sn35 BHEA's surface morphology, resulting in poor surface quality and cracks. Furthermore, we found severe delamination in Sn35 BHEA. The subsurface generates work hardening owing to its dislocation motion, rearrangement, and grain refinement. However, once deformed, dislocation accumulation occurred to a certain extent, resulting in crack formation and, finally, delamination. The absence of obvious work hardening for Sn30 BHEA (Figure 7) was due to its higher material loss rate. This consecutive deformation can be easily induced through delamination [50].

3.4. Corrosion Property Characterization of Sn30 BHEA and Sn35 BHEA

The corrosion resistance properties of biomedical materials during their implantation into the human body is another aspect that needs to be studied. Figure 9 shows the impedance spectroscopy of Sn30 BHEA and Sn35 BHEA, Figure 9a is the Nyquist diagram, and Figure 9b shows the Bode diagram. The electrochemical AC impedance value can reflect the corrosion resistance of the alloy to a certain extent. The greater the impedance value, the better the corrosion resistance. It can be seen from Figure 9a that the capacitive arc curvature radius of Sn30 BHEA decreases significantly, indicating that among the two high-entropy alloys, Sn30 BHEA has the best corrosion resistance; furthermore, it suggests that the decrease in Sn content and the increase in Zr content will improve the corrosion resistance of Sn30 BHEA and Sn35 BHEA. In the Bode diagram, the phase angle of Sn30 BHEA is close to 75° in a wide frequency range, while the phase angle of Sn35 BHEA is about 60°. Sn30 BHEA has a large resistance value and forms a passive film.
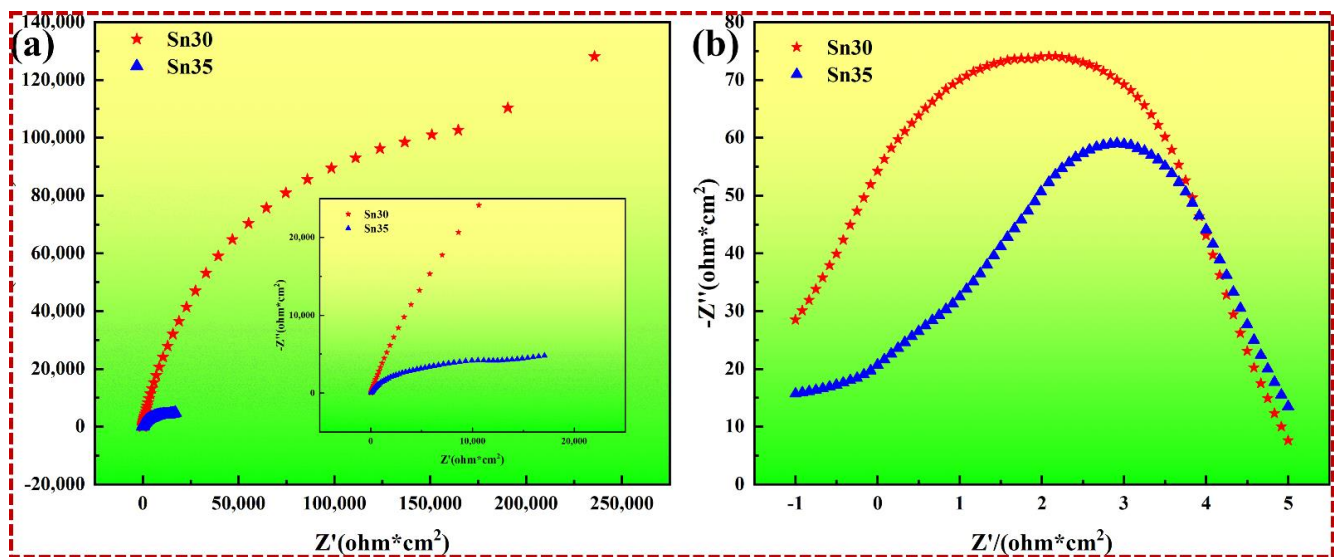
Figure 9. EIS of Sn30 BHEA and Sn35 BHEA: (**a**) Nyquist plots, (**b**) Bode plots.

The potentiodynamic polarization curve and the corrosion morphology of Sn30 BHEA and Sn35 BHEA are shown in Figure 10. The key parameters derived by the Tafel method such as the corrosion current density (I_{corr}) and the corrosion potential (E_{corr}) are listed in Table 4. It was clearly found that Sn30 BHEA exhibited an I_{corr} value smaller than that of Sn35 BHEA. Moreover, for passivation current density I_{pass}, the smaller the value, the easier it is to enter the passivation state. The I_{pass} value of Sn30 BHEA is 4.44×10^{-4} A/cm^{-2}, which is 88% lower than that of Sn35 BHEA—a significant improvement. Another note-worthy fact is that in the anode and cathode area, the value of β_a and β_b of Sn30 BHEA is lower than that of Sn35 BHEA, demonstrating that Sn35 BHEA has stronger corrosion resistance properties. The corrosion potential (E_{corr}) can determine the corrosion trend of the alloy. According to the thermodynamic principle, the smaller the E_{corr}, the greater the corrosion tendency. The E_{corr} of Sn30 HEAs is -0.96, which is about 43.3% smaller than that of Sn35 BHEAs. However, the data that most directly reflect the corrosion resistance of the alloy are the corrosion rate, which can be obtained by the following equation.

$$CR = \frac{0.13 I_{corr} * EW}{d},$$ (1)

where EW is the equivalent weight, and d is the density of the metal (g/cm^3). The calculation results are shown in Table 4. The corrosion rate of Sn30 BHEA is 1.37×10^{-4} mm/a. The corrosion rate of Sn35 BHEA is 1.20×10^{-3} mm/a, which is nearly 88.6% greater than that of ambient pressure. Therefore, Sn30 BHEA has stronger corrosion resistance properties.

Table 4. The key electrochemical parameters of Sn30 BHEA and Sn35 BHEA.

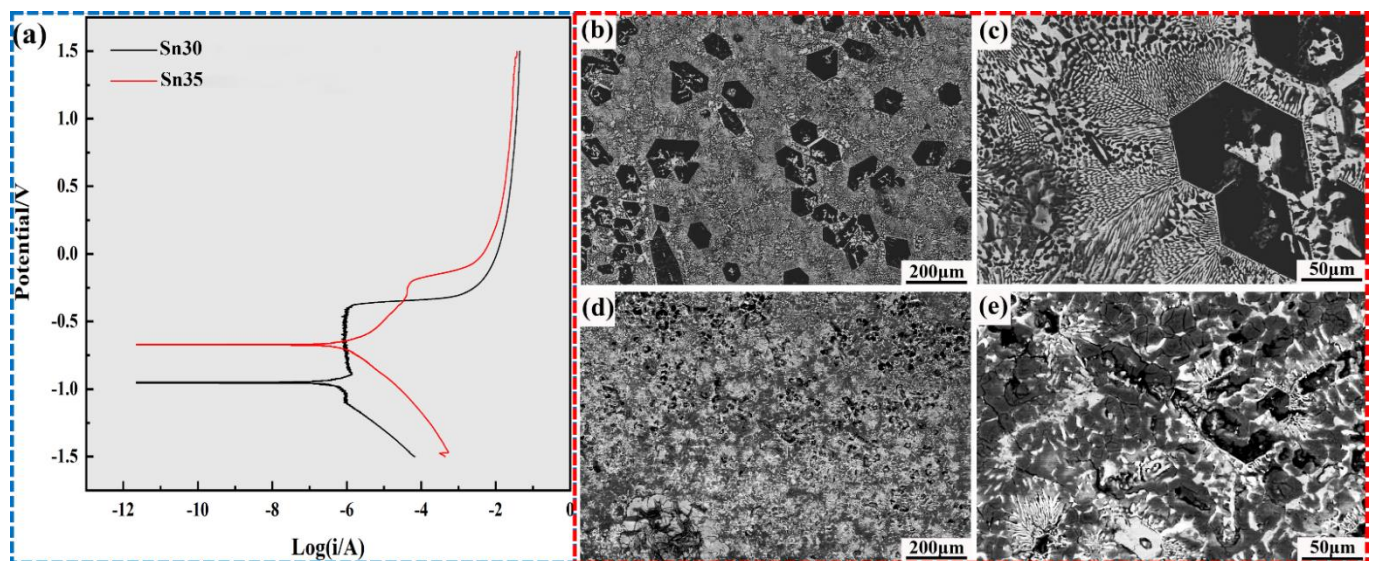| Composition (at.%)	I_{corr} (A/cm^2)	E_{corr} (V)	β_a	β_c	I_{pass} (A/cm^{-2})	Corrosion Rate (mm/a)
Sn30 BHEA	1.261×10^{-7}	-0.96	0.36	0.21	4.44×10^{-4}	1.37×10^{-4}
Sn35 BHEA	1.265×10^{-6}	-0.67	0.76	0.88	3.71×10^{-3}	1.20×10^{-3}

Figure 10. Corrosion properties characterization for Sn30 BHEA and Sn35 BHEA: (**a**) potentiodynamic polarization curves, (**b**,**c**) corrosion morphology of Sn30 BHEA, (**d**,**e**) corrosion morphology of Sn35 BHEA.

The corrosion surface morphology was observed by scanning electron microscopy (SEM) after the potentiodynamic polarization test, as shown in Figure 10b,e. The surfaces of these two high-entropy alloys show certain levels of corrosion after electrochemical corrosion for 2400s and the corrosion degree of (Zr, Sn)-rich phase is high. Meanwhile, the corrosion of Sn35 BHEA also mainly occurs in the gray phase, which is accompanied by many irregular corrosion pits and some cracks. There are also some electrochemical corrosion products on the surface, as shown in Figure 10d,e. The volume fractions of large dendritic Zr-rich zones within Sn30 BHEA and Sn35 BHEA are 77.7% and 90.8% (Figure 11), respectively. Then, from the corrosion morphology and analysis of the above two high-entropy alloys, it can be concluded that the corrosion resistance of Sn30 BHEA is better than that of Sn30 BHEA. However, both alloys exhibit high levels of corrosion resistance [51], indicating that Sn30 BHEA and Sn35 BHEA are a suitable alternative material considering corrosion resistance.
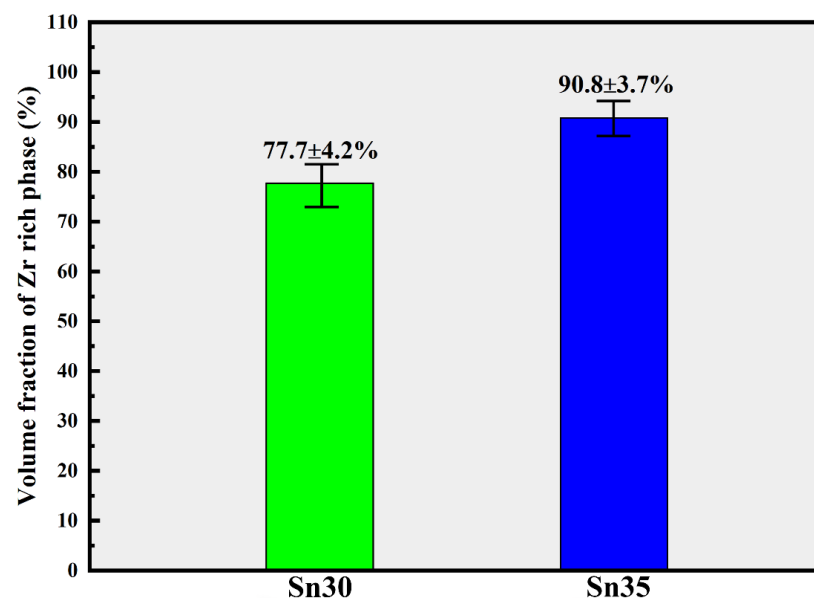

Figure 11. Volume fraction of Zr-rich phase in Sn30 BHEA and Sn35 BHEA.

4. Discussion

According to our SEM results for the surface of the corroded coatings, all of the corroded alloys exhibited similar surface morphologies, i.e., corrosion at the (Zr, Sn)-rich location. The volume fraction of the (Zr, Sn)-rich phase in Sn30 BHEA is smaller than in Sn35 BHEA (Figure 11). Combining the results of our electrochemistry corrosion analysis, we discovered that decreases in the anti-corrosion properties of Sn35 BHEA were due to the increases in the volume fraction of the (Zr, Sn)-rich phase. Moreover, the hardness of Sn30 BHEA is greater than Sn35 BHEA. However, as Sn35 BHEA exhibits a near-eutectic microstructure, it shows excellent plasticity, which, in turn, leads to the best compression strength.

The anti-wear properties are concerned with the alloy's surface quality, hardness, toughness, and loading capability [52–55]. Besides the different anti-wear properties of Sn30 BHEA and Sn35 BHEA, the hardness of each alloy is the key factor related to wear resistance. The hardness of Sn30 BHEA is greater than that of Sn35 BHEA because the volume fraction of the Ta-rich BCC phase is extensively generated (Figure 11). Moreover, during the sliding wear process, the hard Si_3N_4 ball will act similar to a cutter tool and peel off the surface materials, leading to severe plastic deformation and a high wear rate. In addition, the surface's severe wear and damage is accompanied by oxidation under the high-speed wear process. However, for Sn30 BHEA, wear resistance is considerably improved because of the large number of BCC phases generated, which could act as strengthening support sites and carry loads during the wear process. To sum up, Sn30 BHEA shows excellent comprehensive properties. We also conclude that too many Sn elements are not conducive to TiZrTaNbSn HEA design.

5. Conclusions

Taking β-type titanium alloy as the design conception, the comprehensive properties of biomedical high-entropy alloy based on Ti-Zr-Nb-Ta and Sn element were systematically discussed. The main conclusions are as follows:

1. Sn30 BHEA and Sn35 BHEA are typical hypo-eutectic and eutectic structures, respectively, and both alloys are composed of BCC and FCC phases;
2. the two high-entropy alloys have brittle fractures at room temperature. The maximum strain value and compressive strength of Sn30 BHEA are 46.6% and 684.5 MPa, respectively, while the maximum strain value and compressive strength of Sn35 BHEA are 49.9% and 999.2 MPa, respectively. Sn30 HEA's strength and yield strength are better than those of Sn35 HEA;
3. the friction coefficient of Sn30 BHEA is 0.152, the specific and linear wear rates (K_v and K_2, respectively) are 2.27×10^{-4} (mm^3/nm) and 1.163 (mm^3/km), respectively, while the width of the furrow groove is the smallest and shallowest, with almost no wear debris. Furthermore, the friction coefficient of Sn35 BHEA is 0.264, and the values of specific and linear wear (K_v and K_2, respectively), in addition to wear resistance E, are 2.49×10^{-4} (mm^3/nm), 1.277 (mm^3/km), and 0.78 (km/mm^3), respectively. Furthermore, the width of the furrow groove is the largest and deepest, and there are wear debris. In conclusion, the Sn30 HEA has excellent wear resistance and rates compared with Sn35 HEA;
4. Sn30 BHEA has the highest impedance value. The corrosion current density I_{corr} is 1.261×10^{-7} (A/cm^2), which is lower than that of Sn35 BHEA by about 88%. The capacitive arc curvature radius of Sn30 BHEA also considerably decreases. Therefore, Sn30 HEAs preferentially produce passivated film with a small corrosion tendency, indicating that its corrosion resistance is considerably better than that of Sn35 BHEA alloy.

Institutional Review Board Statement: Not applicable.

Informed Consent Statement: Not applicable.

Data Availability Statement: The authors confirm that the data supporting the findings of this study are available within the article.

Conflicts of Interest: The authors declare no conflict of interest.

References

1. Chen, Q.; Thouas, G.A. Metallic implant biomaterials. *Mater. Sci. Eng. R Rep.* **2015**, *87*, 1–57. [CrossRef]
2. Niinomi, M. Recent Metallic Materials for Biomedical Applications. *Metall. Mater. Trans. A* **2002**, *33*, 477–486. [CrossRef]
3. Long, M.; Rack, H.J. Titanium alloys in total joint replacement—A materials science perspective. *Biomaterials* **1998**, *19*, 1621–1636. [CrossRef]
4. Okuno, O.; Takayuki, J.; Hamavaka, H. Titanium Alloys in Dental and Medical Field. *J. Lron Steel Inst. Jpn.* **1990**, *76*, 1633–1641. [CrossRef]
5. Bordji, K.; Jouzeau, J.Y.; Mainard, D.; Payan, E.; Netter, P.; Rie, K.T.; Stucky, T.; Hage-Ali, M. Cytocompatibility of Ti-6Al-4V and Ti-5Al-2.5Fe alloys according to three surface treatments, using human fibroblasts and osteoblasts. *Biomaterials* **1996**, *17*, 929–940. [CrossRef]
6. Liu, W.; Liu, S.; Wang, L. Surface Modification of Biomedical Titanium Alloy: Micromorphology, Microstructure Evolution and Biomedical Applications. *Coatings* **2019**, *9*, 249. [CrossRef]
7. Gnedenkov, S.V.; Sinebryukhov, S.L.; Puz', A.V.; Egorkin, V.S.; Kostiv, R.E. In vivo study of osteogenerating properties of calcium-phosphate coating on titanium alloy Ti–6Al–4V. *Bio-Med. Mater. Eng.* **2017**, *27*, 551–560. [CrossRef]
8. Chen, T.K.; Shun, T.T.; Yeh, J.W.; Wong, M.S. Nanostructured nitride films of multi-element high-entropy alloys by reactive DC sputtering. *Surf. Coat. Technol.* **2004**, *188*, 193–200. [CrossRef]
9. Yeh, J.W.; Lin, S.J.; Chin, T.S.; Gan, J.Y.; Chen, S.K.; Shun, T.T.; Tsau, C.H.; Chou, S.Y. Formation of simple crystal structures in Cu-Co-Ni-Cr-Al-Fe-Ti-V alloys with multiprincipal metallic elements. *Metall. Mater. Trans. A* **2004**, *35*, 2533–2536. [CrossRef]
10. Yeh, J.W.; Chen, S.K.; Lin, S.J.; Gan, J.Y.; Chin, S.Y.; Shun, T.T.; Tsau, C.H.; Chang, S.Y. Nanostructured high-entropy al-loys with multiple principal elements: Novel alloy design concepts and outcomes. *Adv. Eng. Mater.* **2004**, *6*, 299. [CrossRef]
11. George, E.P.; Raabe, D.; Ritchie, R.O. High-entropy alloys. *Nat. Rev. Mater.* **2019**, *41578*, 515–534. [CrossRef]
12. Akrami, S.; Edalati, P.; Fuji, M.; Edalati, K. High-entropy ceramics: Review of principles, production and applications. *Mater. Sci. Eng. R Rep.* **2021**, *146*, 100644. [CrossRef]
13. Zhang, Z.Q.; Ketov, S.V.; Fellner, S.; Sheng, H.P.; Mitterer, C.; Song, K.K.; Gammer, C.; Eckert, J. Reactive interdiffusion of an Al film and a CoCrFeNi high-entropy alloy. *Mater. Des.* **2022**, *216*, 110530. [CrossRef]
14. Singh, S.K.; Parashar, A. Atomistic simulations to study crack tip behaviour in multi-elemental alloys. *Eng. Fract. Mech.* **2021**, *243*, 107536. [CrossRef]
15. Chang, C.C.; Hsiao, Y.T.; Chen, Y.L.; Tsai, C.Y.; Lee, Y.J.; Ko, P.H.; Chang, S.Y. Lattice distortion or cocktail effect dominates the performance of Tantalum-based high-entropy nitride coatings. *Appl. Surf. Sci.* **2022**, *577*, 151894. [CrossRef]
16. Chen, C.; Yuan, S.; Chen, J.; Wang, W.; Zhang, W.; Wei, R.; Wang, T.; Zhang, T.; Guan, S.; Li, F. A Co-free Cr-Fe-Ni-Al-Si high-entropy alloy with outstanding corrosion resistance and high hardness fabricated by laser surface melting. *Mater. Lett.* **2022**, *314*, 131882. [CrossRef]
17. Jiao, W.; Li, T.; Chang, X.; Lu, Y.; Yin, G.; Cao, Z.; Li, T. A novel Co-free Al$_{0.75}$CrFeNi eutectic high-entropy alloy with superior mechanical properties. *J. Alloys Compd.* **2022**, *902*, 163814. [CrossRef]
18. Cui, P.; Bao, Z.; Liu, Y.; Zhou, F.; Lai, Z.; Zhou, Y.; Zhu, J. Corrosion behavior and mechanism of dual phase Fe$_{1.125}$Ni$_{1.06}$CrAl high-entropy alloy. *Corros. Sci.* **2022**, *201*, 110276. [CrossRef]
19. Kong, D.; Wang, W.; Zhang, T.; Guo, J. Effect of superheating on microstructure and wear resistance of Al$_{1.8}$CrCuFeNi$_2$ high-entropy alloy. *Mater. Lett.* **2022**, *311*, 131613. [CrossRef]
20. Miracle, D.B.; Senkov, O.N. A critical review of high entropy alloys and related concepts. *Acta Mater.* **2017**, *122*, 448. [CrossRef]

21. Yuan, Y.; Wu, Y.; Yang, Z.; Liang, X.; Lei, Z.; Huang, H.; Wang, H.; Liu, X.; An, K.; Wu, W.; et al. Formation, structure and properties of biocompatible TiZrHfNbTa high-entropy alloys. *Mater. Res. Lett.* **2019**, *7*, 225–231. [CrossRef]

22. Senkov, O.N.; Scott, J.M.; Senkova, S.V.; Miracle, D.B.; Woodward, C.F. Microstructure and room temperature properties of a high-entropy TaNbHfZrTi alloy. *J. Alloys Compd.* **2011**, *509*, 6043–6048. [CrossRef]

23. Dirras, G.; Lilensten, L.; Djemia, P.; Laurent-Brocq, M.; Tingaud, D.; Couzinie, J.P.; Perrie're, L.; Chauveau, T.; Guillot, I. Elastic and plastic properties of as-cast equimolar TiHfZrTaNb high-entropy alloy. *Mater. Sci. Eng. A* **2016**, *654*, 30–38. [CrossRef]

24. Motallebzadeh, A.; Peighambardoust, N.S.; Sheikh, S.; Murakami, H.; Guo, S. Demircan Canadinc Microstructural, mechanical and electrochemical characterization of TiZrTaHfNb and Ti$_{1.5}$ZrTa$_{0.5}$Hf$_{0.5}$Nb$_{0.5}$ refractory high-entropy alloys for biomedical applications. *Intermetallics* **2019**, *113*, 106572. [CrossRef]

25. Yang, W.; Liu, Y.; Pang, S.; Liaw, P.K.; Zhang, T. Bio-corrosion behavior and in vitro biocompatibility of equimolar TiZrHfNbTa high-entropy alloy. *Intermetallics* **2020**, *124*, 106845. [CrossRef]

26. Wang, S.; Xu, J. TiZrNbTaMo high-entropy alloy designed for orthopedic implants: As-cast microstructure and mechanical properties. *Mater. Sci. Eng. C* **2017**, *73*, 80–89. [CrossRef] [PubMed]

27. Mitsuharu, T.; Takeshi, N.; Takao, H.; Aira, M.; Aiko, S.; Takayoshi, N. Novel TiNbTaZrMo high-entropy alloys for metallic biomaterials. *Scr. Mater.* **2017**, *129*, 65–68.

28. Hua, N.; Wang, W.; Wang, Q.; Ye, Y.; Lin, S.; Zhang, L.; Guo, Q.; Brechtl, J.; Liaw, P.K. Mechanical, corrosion, and wear properties of biomedical Ti-Zr-Nb-Ta-Mo high entropy alloys. *J. Alloys Compd.* **2021**, *861*, 157997. [CrossRef]

29. Takao, H.; Takeshi, N.; Mitsuharu, T.; Aira, M.; Takayoshi, N. Development of non-equiatomic Ti-Nb-Ta-Zr-Mo high-entropy alloys for metallic biomaterials. *Scr. Mater.* **2019**, *172*, 83–87.

30. Juan, C.C.; Tsai, M.H.; Tsai, C.W.; Lin, C.M.; Wang, W.R.; Yang, C.C.; Chen, S.K.; Lin, S.J.; Yeh, J.W. Enhanced mechanical properties of HfMoTaTiZr and HfMoNbTaTiZr refractory high-entropy alloys. *Intermetallics* **2015**, *62*, 76. [CrossRef]

31. Yuuka, L.; Takeshi, N.; Aira, M.; Pan, W.; Kei, A.; Takanoshi, N. Design and development of Ti-Zr-Hf-Nb-Ta-Mo high-entropy alloys for metallic biomaterials. *Mater. Des.* **2021**, *202*, 109548.

32. Zhang, Y.; Zuo, T.; Tang, Z.; Gao, M.C.; Dahmen, K.A.; Liaw, P.K.; Lu, Z.P. Microstructures and properties of high-entropy alloys. *Prog. Mater. Sci. Forum* **2014**, *61*, 1–93. [CrossRef]

33. Lei, Z.; Liu, X.; Wu, Y.; Wang, H.; Jiang, S.; Wang, S.; Hui, X.; Wu, Y.; Gault, B.; Kontis, P.; et al. Enhanced strength and ductility in a high-entropy alloy via ordered oxygen complexes. *Nature* **2018**, *563*, 546–550. [CrossRef] [PubMed]

34. Mariana, C.; Jithin, V.; Pramote, T.; Mihaela, P.M.; Maria, K.; Geetha, M.; Annett, G. Tailoring biocompatible Ti-Zr-Nb-Hf-Si metallic glasses based on high-entropy alloys design approach. *Mater. Sci. Eng. C* **2021**, *121*, 111733.

35. Huang, L.; Long, M.; Liu, W.; Li, S. Effects of Cr on microstructure, mechanical properties and hydrogen desorption behaviors of ZrTiNbMoCr high entropy alloys. *Mater. Lett.* **2021**, *293*, 129718. [CrossRef]

36. Liu, L.; Zhu, J.B.; Zhang, C.; Li, J.C.; Jiang, Q. Microstructure and the properties of FeCoCuNiSnx high entropy alloys. *Mater. Sci. Eng. A* **2012**, *548*, 64–68. [CrossRef]

37. Liu, L.; Zhu, J.B.; Li, L.; Li, J.C.; Jiang, Q. Microstructure and tensile properties of FeMnNiCuCoSnx high entropy alloys. *Mater. Des.* **2013**, *44*, 223. [CrossRef]

38. Gutierrez-Moreno, J.J.; Guo, Y.; Georgarakis, K.; Yavari, A.R.; Evangelakis, G.A.; Lekka, C.E. The role of Sn doping in the ß-type Ti-25at%Nb alloys: Experiment and ab initio calculations. *J. Alloys Compd.* **2014**, *615*, 676–679. [CrossRef]

39. Miura, K.; Yamada, N.; Hanada, S.; Jung, T.; Itoi, E. The bone tissue compatibility of a new Ti-Nb-Sn alloy with a low Young's modulus. *Acta Biomater.* **2011**, *7*, 2320–2326. [CrossRef]

40. Moraes, P.E.L.; Contieri, R.J.; Lopes, E.S.N.; Robin, A.; Caram, R. Effects of Sn addition on the microstructure, mechanical properties and corrosion behavior of Ti-Nb-Sn alloys. *Mater. Charact.* **2014**, *96*, 273–281. [CrossRef]

41. Zheng, Y.F.; Wang, B.L.; Wang, J.G.; Li, C.; Zhao, L.C. Corrosion behaviour of Ti-Nb-Sn shape memory alloys in different simulated body solutions. *Mater. Sci. Eng. A* **2006**, *438*, 891–895. [CrossRef]

42. Ma, T.; Li, Q.; Jin, Y.; Zhao, X.; Wang, X.; Dong, D.; Zhu, D.D. As-cast microstructure and properties of none-qual atomic ratio TiZrTaNbSn high entropy alloys. *China Foundry* **2022**, 1–8.

43. Han, L.; Mu, J.; Zhou, Y.; Zhu, Z.; Zhang, H. Effect of Heat Treatment Temperature on Microstructure and Mechanical Properties of Ti$_{0.5}$Zr$_{1.5}$NbTa$_{0.5}$Sn$_{0.2}$ High-Entropy Alloy. *Acta Met. Sin* **2022**, *582*, 1159–1168.

44. Jung, Y.; Lee, K.; Hong, S.J.; Lee, J.K.; Han, J.; Kim, K.B.; Liaw, P.K.; Lee, C.O.L.; Song, G. Investigation of phase-transformation path in TiZrHf(VNbTa)x refractory high-entropy alloys and its effect on mechanical property. *J. Alloys Compd.* **2021**, *886*, 161187. [CrossRef]

45. Gurel, S.; Yagci, M.B.; Canadinc, D.; Gerstein, G.; Bal, B.; Maier, H.J. Fracture behavior of novel biomedical Ti-based high entropy alloys under impact loading. *Mater. Sci. Eng. A* **2021**, *1*, 803. [CrossRef]

46. Cheng, J.; Yang, J.; Zhang, X.; Zhong, H.; Ma, J.; Li, F.; Fu, L.; Bi, Q.; Li, J.; Liu, W. High temperature tribological behavior of a Ti-46Al-2Cr-2Nb intermetallics. *Intermetallics* **2012**, *31*, 120–126. [CrossRef]

47. García-Martínez, E.; Miguel, V.; Martínez, A.; Naranjo, J.A.; Coello, J. Tribological characterization of tribosystem Ti48Al2Cr2Nb-coated/uncoated carbide tools at different temperatures. *Wear* **2021**, *484–485*, 203992. [CrossRef]

48. Mengis, L.; Grimme, C.; Galetz, M.C. Tribological properties of the uncoated and aluminized Ti–48Al–2Cr–Nb TiAl alloy at high temperatures. *Wear* **2021**, *477*, 203818. [CrossRef]

49. Shi, X.; Yao, J.; Xu, Z.; Zhai, W.; Song, S.; Wang, M.; Zhang, Q. Tribological performance of TiAl matrix self-lubricating composites containing Ag, Ti$_3$SiC$_2$ and BaF$_2$/CaF$_2$ tested from room temperature to 600 °C. *Mater. Des.* **2014**, *53*, 620–633. [CrossRef]

50. Wang, Z.; Yan, Y.; Wu, Y.; Su, Y.; Qiao, L. Repassivation and dry sliding wear behavior of equiatomic medium entropy TiZr (Hf, Ta, Nb) alloys. *Mater. Lett.* **2022**, *312*, 131643. [CrossRef]

51. Tang, Z.; Huang, L.; He, W.; Liaw, P. Alloying and processing effects on the Aqueous corrosion behavior of high entropy alloys. *Entropy* **2014**, *16*, 895–911. [CrossRef]

52. Allahyarzadeh, M.H.; Aliofkhazraei, M.; Rouhaghdam, A.R.S.; Torabinejad, V. Structure and wettability of pulsed electrodeposited Ni-W-Cu-(α-alumina) nanocomposite. *Surf. Coat. Technol.* **2016**, *307*, 525–533. [CrossRef]

53. Allahyarzadeh, M.H.; Aliofkhazraeia, M.; Rouhaghdam, A.S.; Alimadadi, H.; Torabinejad, V. Mechanical properties and load bearing capability of nanocrystalline nickel-tungsten multilayered coatings. *Surf. Coat. Technol.* **2020**, *386*, 125472. [CrossRef]

54. Rupert, T.J.; Schuh, C.A. Sliding wear of nanocrystalline Ni–W: Structural evolution and the apparent breakdown of archard scaling. *Acta Mater.* **2010**, *58*, 4137–4148. [CrossRef]

55. Maharana, H.S.; Mondal, K. Manifestation of Hall–Petch breakdown in nanocrystalline electrodeposited Ni-MoS$_2$ coating and its structure dependent wear resistance behavior. *Surf. Coat. Technol.* **2021**, *410*, 126950. [CrossRef]